



# Subgrid-scale helicity equation model for large-eddy simulation of turbulent flows

Cite as: Phys. Fluids **33**, 035128 (2021); <https://doi.org/10.1063/5.0038165>

Submitted: 19 November 2020 • Accepted: 28 January 2021 • Published Online: 09 March 2021

 Han Qi (齐涵),  Xinliang Li (李新亮) and Changping Yu (于长平)



View Online



Export Citation



CrossMark

## ARTICLES YOU MAY BE INTERESTED IN

### [Referee acknowledgment for 2020](#)

Physics of Fluids **33**, 020201 (2021); <https://doi.org/10.1063/5.0043282>

### [Impact of numerical hydrodynamics in turbulent mixing transition simulations](#)

Physics of Fluids **33**, 035126 (2021); <https://doi.org/10.1063/5.0034983>

### [Implicit large-eddy simulations of turbulent flow in a channel via spectral/hp element methods](#)

Physics of Fluids **33**, 035130 (2021); <https://doi.org/10.1063/5.0040845>

APL Machine Learning

Open, quality research for the networking communities

OPEN FOR SUBMISSIONS MAY 2022

LEARN MORE



# Subgrid-scale helicity equation model for large-eddy simulation of turbulent flows

Cite as: Phys. Fluids **33**, 035128 (2021); doi: [10.1063/5.0038165](https://doi.org/10.1063/5.0038165)

Submitted: 19 November 2020 · Accepted: 28 January 2021 ·

Published Online: 9 March 2021





View Online



Export Citation



CrossMark

Han Qi (齐涵),<sup>1,2</sup>  Xinliang Li (李新亮),<sup>1,2</sup>  and Changping Yu (于长平)<sup>1,a)</sup>

## AFFILIATIONS

<sup>1</sup>LHD, Institute of Mechanics, Chinese Academy of Sciences, Beijing 100190, China

<sup>2</sup>School of Engineering Science, University of Chinese Academy of Sciences, Beijing 100049, China

<sup>a)</sup>Author to whom correspondence should be addressed: [cpyu@imech.ac.cn](mailto:cpyu@imech.ac.cn)

## ABSTRACT

A new one-equation eddy-viscosity model based on subgrid-scale (SGS) helicity is introduced in this paper for large-eddy simulation (LES) of turbulent flows. First, the governing equation of SGS helicity is deduced from the incompressible Navier–Stokes equations, and it reflects the transfer of the small-scale helicity that has been filtered out. We deduce a certain functional relation between the eddy viscosity and SGS helicity based on the kinetic energy and helicity spectra in the homogeneous and isotropic helical turbulence. For improving the accuracy, each unclosed term in the governing equation of SGS helicity is modeled independently, and the coefficients of these unclosed terms are constants or are determined dynamically. The new one-equation eddy-viscosity model is first tested and validated in the simulation of the homogeneous and isotropic helical turbulence. The *a priori* tests from the direct numerical simulation of forced homogeneous and isotropic turbulence show that the energy and helicity fluxes exhibit scale invariance in the inertial subrange. Additionally, the *a posteriori* tests demonstrate that the constant-coefficient and dynamic SGS helicity equation models can predict both the energy and helicity spectra more precisely than the common SGS models. For the LES of channel flow, the SGS helicity equation model can accurately predict the mean velocity, the turbulent stress, and the viscous shear stress and supply more abundant flow structures than the compared SGS model under the same grid resolution.

Published under license by AIP Publishing. <https://doi.org/10.1063/5.0038165>

## I. INTRODUCTION

Large-eddy simulation (LES) plays an important role in the numerical simulation of turbulent flows, specifically in high Reynolds number turbulence. Through low-pass filtering of the Navier–Stokes equations, the small-scale field is filtered out, and the filtered Navier–Stokes equations exhibit an unclosed term, which is the subgrid-scale (SGS) stress.

In the current LES, a commonly used SGS stress model is the eddy-viscosity model. The constant-coefficient Smagorinsky model (SM) is the first SGS eddy-viscosity model proposed by Smagorinsky<sup>1</sup> and Lilly.<sup>2</sup> Chollet<sup>3</sup> suggested the spectral eddy-viscosity model based on eddy-damped quasi-normal Markovian theory (EDQNM). Then, the Germano identity<sup>4</sup> was introduced to dynamically calculate the coefficient of the Smagorinsky model, resulting in the current dynamic Smagorinsky model (DSM). By modifying the eddy viscosity of SM to satisfy the near-wall scaling behavior, Nicoud and Ducros<sup>5</sup> proposed a wall-adapting local eddy viscosity (WALE) model, which can improve the prediction of the wall stress rate.

Vreman<sup>6</sup> proposed an eddy-viscosity model (Vreman model). Its eddy viscosity can vanish when the SGS dissipation trends to zero,

which guarantees to predict turbulence and transitional flow adequately. The SGS kinetic energy transport equation was introduced by Schumann<sup>7</sup> to solve the eddy viscosity of the SGS stress model (*k*-equation model), and it succeeded in predicting turbulent channel flow. With the aid of the statistical results obtained from the two-scale direct interaction approximation (DIA), Yoshizawa<sup>8</sup> constructed an SGS kinetic energy model and determined the experiential coefficients of the modeled terms in the SGS kinetic energy transport equation, which is the most commonly used one-equation SGS model. Ghosal *et al.*<sup>9</sup> applied the dynamic procedure to the SGS kinetic energy models (*dk*-equation), and the coefficients of the one-equation model can be determined dynamically. The dynamic one-equation model can effectively improve the prediction results of high Reynolds number turbulence. Using the infinite series expansions for the unclosed terms, Pomraning and Rutland<sup>10</sup> suggested a new dynamic one-equation non-viscosity LES model. With the aid of the SGS kinetic energy transfer equation, Chai and Mahesh<sup>11</sup> presented a new dynamic eddy-viscosity model for large eddy simulation of compressible turbulence. In addition to the eddy-viscosity model, there are still some other types

of SGS models. Based on the scale similarity hypothesis, Bardina *et al.*<sup>12</sup> and Liu *et al.*<sup>13</sup> obtained the scale similarity model. Considering the subgrid geometrical eddy structure, Misra<sup>14</sup> proposed the stretched-vortex model. Clark *et al.*<sup>15</sup> and Vreman *et al.*<sup>16</sup> put forward the gradient model (GM) using different expansion methods.

Helicity plays an essential role in many natural phenomena, such as hurricanes and tornadoes in geophysical flows. In previous turbulence modeling, more attention was focused on kinetic energy. Helicity, the integral of the scalar product of velocity  $\mathbf{u}$  and vorticity  $\boldsymbol{\omega}$ , is a second quadratic inviscid invariant in addition to kinetic energy in three-dimensional (3D) flows, which means that helicity can cascade to small scales linearly along the energy cascade in 3D turbulence. Helicity reflects certain topological characteristics of the flows, such as knottedness or linkage of vortex lines.<sup>17,18</sup> As is well known, there are cascade phenomena and coherent structures in turbulent flows, which indicates that the use of helicity is an appropriate turbulence modeling approach. Yokoi<sup>19</sup> proposed a three-equation with the turbulent helicity using the theoretical results for Reynolds average Navier–Stokes. Then Baerenzung *et al.*<sup>20</sup> obtained a dynamical spectral model for large eddy simulation based on EDQNM. They also took into account the turbulent helicity transfers and proposed a helical model. Based on the character of helicity transfer between scales, Yu *et al.*<sup>21</sup> proposed a novel eddy-viscosity model (HM), and the new eddy viscosity is related to the large-scale strain rate tensor and vorticity gradient tensor. Zhou *et al.*<sup>22</sup> proved that the HM could predict transitional flow without explicit filtering.

In existing research, almost all of the one-equation models are based on the SGS kinetic energy. This study will supply the SGS helicity transport equation and then model the unclosed terms of the SGS helicity transport equation ( $h$ -equation model). The coefficients of the unclosed terms can be given directly or solved dynamically. The deduction of the  $h$ -equation model is introduced in Sec. II. In Sec. III, the new model is tested *a priori* and *a posteriori* in the homogeneous and isotropic helicity turbulence (HIHT) and is also tested *a posteriori* in incompressible channel flow.

The results obtained from the  $h$ -equation model are compared with those from SM and DSM. The conclusion and discussion are given in Sec. IV.

## II. GOVERNING EQUATIONS AND THEORETICAL ANALYSIS

### A. The filtered Navier–Stokes equations

In the LES of incompressible turbulent flows, the filtered Navier–Stokes equations are taken as follows:

$$\frac{\partial \bar{u}_i}{\partial t} + \frac{\partial \bar{u}_i \bar{u}_j}{\partial x_j} = -\frac{1}{\rho} \frac{\partial \bar{p}}{\partial x_i} + \nu \frac{\partial^2 \bar{u}_i}{\partial x_j^2} + \bar{f}_i - \frac{\partial \tau_{ij}}{\partial x_j}, \quad (1)$$

where a bar denotes spatial filtering at scale  $\Delta$ ,  $\bar{f}_i$  is the filtered forcing, and  $\tau_{ij} = \bar{u}_i \bar{u}_j - \bar{u}_i \bar{u}_j$  is the SGS stress tensor that needs to be modeled. The filtering operation is represented as  $\bar{\phi}(x) = \int_{-\infty}^{\infty} G(y) \phi(x-y) dy$ , and  $G$  is designated as the “grid filter” function.

### B. Subgrid-scale model

In LES, the eddy viscosity can be written as

$$\tau_{ij}^{mod} - \frac{1}{3} \delta_{ij} \tau_{kk}^{mod} = -2\nu_{sgs} \bar{S}_{ij}, \quad (2)$$

where  $\bar{S}_{ij} = 1/2(\partial_j \bar{u}_i + \partial_i \bar{u}_j)$  is the resolved (velocity) strain rate tensor, and  $\nu_{sgs}$  is the SGS viscosity, which needs to be modeled.

In the Smagorinsky model (SM), the SGS viscosity is proposed as

$$\nu_{sgs} = (C_s \Delta)^2 |\bar{S}|, \quad (3)$$

with

$$|\bar{S}| = \sqrt{2\bar{S}_{ij}\bar{S}_{ij}}, \quad (4)$$

where the constant  $C_s$  is suggested to be 0.18 in incompressible turbulence.

The traditional dynamic model requires a test filtering operation on the filtered field, which is denoted by *tilde*, and the subtest-scale (STS) stress tensor is

$$T_{ij} = \widetilde{\bar{u}_i \bar{u}_j} - \widetilde{\bar{u}_i} \widetilde{\bar{u}_j}. \quad (5)$$

Although  $T_{ij}$  and  $\tau_{ij}$  are unknown in LES, the two tensors are related by the Germano identity

$$L_{ij} = T_{ij} - \widetilde{\tau}_{ij}, \quad (6)$$

where  $L_{ij} = \widetilde{\bar{u}_i \bar{u}_j} - \widetilde{\bar{u}_i} \widetilde{\bar{u}_j}$  is the Leonard term. Then, for DSM, the Germano identity can be rewritten as

$$L_{ij} - \frac{1}{3} L_{kk} \delta_{ij} = -2C_s \left[ \widetilde{\Delta^2 |\bar{S}| \bar{S}_{ij}} - \Delta^2 |\widetilde{\bar{S}}| \widetilde{\bar{S}_{ij}} \right]. \quad (7)$$

Using Germano identity, the coefficient of DSM can be obtained as

$$C_s = \frac{\langle M_{ij} L_{ij} \rangle}{\langle M_{ij} M_{ij} \rangle}, \quad (8)$$

where  $M_{ij} = [\Delta^2 |\widetilde{\bar{S}}| \widetilde{\bar{S}_{ij}} - \widetilde{\Delta^2 |\bar{S}| \bar{S}_{ij}}]$ .

### C. Derivation of eddy viscosity based on SGS helicity

For turbulent flows, we define the SGS helicity as  $h_{sgs} = (\mathbf{u}_i - \bar{u}_i)(\boldsymbol{\omega}_i - \bar{\boldsymbol{\omega}}_i)$ , which may reflect the helicity transfer between the resolved scale and subgrid scale. The ensemble average of the SGS helicity can be written as

$$\langle h_{sgs} \rangle = \langle (\mathbf{u}_i - \bar{u}_i)(\boldsymbol{\omega}_i - \bar{\boldsymbol{\omega}}_i) \rangle. \quad (9)$$

In forced homogeneous and isotropic helical turbulence, there exists a joint cascade of both energy and helicity to smaller scales with Kolmogorov’s  $-5/3$  power-law spectra. The energy spectrum in the inertial subrange is

$$E(k) = C_K \varepsilon^{2/3} k^{-5/3}, \quad (10)$$

where  $\varepsilon$  is the energy dissipation rate and the coefficient  $C_K$  (the Kolmogorov constant for energy) is approximately 1.4.<sup>23</sup> The helicity spectrum in the inertial subrange has the form

$$H(k) = C_H \eta \varepsilon^{-1/3} k^{-5/3}, \quad (11)$$

where  $\eta$  is the helicity dissipation rate and the coefficient  $C_H$  (the Kolmogorov constant for helicity) is approximately 1.0.<sup>23</sup>

In the case of an inertial subrange extending to infinity beyond the cutoff, we have the relation

$$\langle h_{sgs} \rangle = \int_{k_c}^{\infty} H(k) dk = \frac{3}{2} C_H \eta \varepsilon^{-1/3} k_c^{-2/3}, \quad (12)$$

where  $k_c = \pi/\Delta$  is the cutoff wavenumber.

In helical turbulence, the spectral relative helicity is defined as

$$\alpha(k) = \frac{|H(k)|}{2kE(k)}, \quad (13)$$

which measures the ratio of the square of a distortion time scale for the helicity cascade and that for the energy cascade. The existing research has shown that the spectral relative helicity  $\alpha(k)$  must decay with increasing wavenumber  $k$  and that the mean spectral relative helicity should scale as  $k^{-1}$  in the inertial subrange in both direct numerical simulation (DNS) and LES.

In a statistically steady state,  $\alpha$  usually varies between 0 and 1 with wavenumber  $k$ .<sup>24</sup> Then, such a relationship can be obtained as

$$\varepsilon = \frac{C_H}{C_K} (2\alpha k)^{-1} |\eta|. \quad (14)$$

If one lets  $k = k_c$ , the helicity dissipation rate will take the form

$$|\eta| = \frac{C_K}{C_H} 2\alpha k_c \varepsilon. \quad (15)$$

Substituting Eq. (15) into Eq. (12), one can obtain the relationship between the SGS helicity and the energy dissipation rate in the form

$$|\langle h_{sgs} \rangle| = 3C_K \alpha k_c^{1/3} \varepsilon^{2/3}. \quad (16)$$

The relationship between the energy dissipation rate and the SGS eddy viscosity<sup>25</sup> is

$$\nu_{sgs} = \frac{A}{C_K \pi^{4/3}} \varepsilon^{1/3} \Delta^{4/3}. \quad (17)$$

By means of Eq. (16) and Eq. (17), the new eddy viscosity can be derived as

$$\nu_{sgs} = C_{he} \Delta^{3/2} |\langle h_{sgs} \rangle|^{1/2}, \quad (18)$$

where  $C_{he} = A/(\sqrt{3}C_K^{3/2}\alpha^{1/2}\pi^{7/6})$  is the coefficient of the eddy viscosity. As suggested by Sagaut,<sup>25</sup>  $A$  can be chosen as 0.438. Therefore, the coefficient  $C_{he}$  is chosen as 0.037 in incompressible flows.

To take into account the pointwise correlation between the SGS stress tensor and the resolved strain rate tensor, the local eddy viscosity can be regarded as

$$\nu_{sgs} = C_{he} \Delta^{3/2} |h_{sgs}|^{1/2}. \quad (19)$$

In Eq. (19), the absolute value of subgrid-scale helicity is used. Thus in some cases where the values of the averaged helicity are zero,<sup>26</sup> the new model can also be employed.

For simplicity, the generalized SGS helicity can be defined as

$$h_s = \overline{u_i \omega_i} - \overline{u_i} \overline{\omega_i}. \quad (20)$$

If the filter is a Reynolds operator, the generalized SGS helicity is equal to the SGS helicity.<sup>25</sup> In practice,  $h_s$  is used to compute the SGS eddy viscosity. And thus, we use  $h_s$  to represent the SGS helicity in this paper.

#### D. Transport equation of SGS helicity

From the Navier–Stokes equation of incompressible turbulence, the transport equation of helicity can be derived as

$$\frac{\partial h}{\partial t} + \frac{\partial u_j h}{\partial x_j} = \frac{\partial Q_j}{\partial x_j} - 4\nu S_{ij} R_{ij} + 2f_i \omega_i, \quad (21)$$

where  $h = \mathbf{u} \cdot \boldsymbol{\omega}$ ,  $R_{ij} = \frac{1}{2}(\partial \omega_i / \partial x_j + \partial \omega_j / \partial x_i)$  is the symmetric part of the vorticity gradient tensor, and  $Q_i$  is the spatial transport term

$$Q_j = -\frac{p}{\rho} \omega_j + \frac{1}{2} u_i u_i \omega_j + 2\nu u_i R_{ij} + 2\nu \omega_i S_{ij} - \varepsilon_{jkm} u_k f_m. \quad (22)$$

We define the resolved helicity as  $h_\Delta = \bar{\mathbf{u}} \cdot \bar{\boldsymbol{\omega}}$ , where  $h_\Delta$  satisfies the following equation:

$$\frac{\partial h_\Delta}{\partial t} + \frac{\partial \bar{u}_j h}{\partial x_j} = \frac{\partial \bar{Q}_j}{\partial x_j} - \Pi_\Delta^H - 4\nu \bar{S}_{ij} \bar{R}_{ij} + 2\bar{f}_i \bar{\omega}_i, \quad (23)$$

where  $\Pi_\Delta^H = -2\tau_{ij} \bar{R}_{ij}$  is the SGS helicity dissipation rate and  $\bar{Q}_j$  is the spatial transport term at scale  $\Delta$

$$\begin{aligned} \bar{Q}_j = & -2\bar{\omega}_i \tau_{ij} - \varepsilon_{ijk} \bar{u}_i \frac{\partial \tau_{kl}}{\partial x_l} - \frac{\bar{p}}{\rho} \bar{\omega}_j + \frac{1}{2} \bar{u}_i \bar{u}_i \bar{\omega}_j \\ & + 2\nu (\bar{u}_i \bar{R}_{ij} + \bar{\omega}_i \bar{S}_{ij}) - \varepsilon_{jkl} \bar{u}_k \bar{f}_l. \end{aligned} \quad (24)$$

Thus, the SGS helicity transport equation ( $h$ -equation) can be derived by subtracting Eq. (23) from the filter Eq. (21) as

$$\begin{aligned} \frac{\partial h_s}{\partial t} + \frac{\partial \bar{u}_j h_s}{\partial x_j} = & -2\tau_{ij} \bar{R}_{ij} + 2 \frac{\partial \bar{\omega}_i \tau_{ij}}{\partial x_j} + 2 \frac{\partial \varepsilon_{ijk} \bar{u}_i \left( \frac{\partial \tau_{kl}}{\partial x_l} \right)}{\partial x_j} \\ & + \nu \frac{\partial^2 h_s}{\partial x_j^2} + Q, \end{aligned} \quad (25)$$

where

$$\begin{aligned} Q = & \frac{\partial \bar{u}_j \bar{u}_i \bar{\omega}_i}{\partial x_j} - \frac{\partial \bar{u}_j \bar{u}_i \bar{\omega}_i}{\partial x_j} - \frac{\partial \left( \frac{1}{\rho} \bar{p} \bar{\omega}_j - \frac{1}{\rho} \bar{p} \bar{\omega}_j \right)}{\partial x_j} \\ & + \frac{1}{2} \frac{\partial (\bar{u}_i \bar{u}_i \bar{\omega}_j - \bar{u}_i \bar{u}_i \bar{\omega}_j)}{\partial x_j} - 2\nu \left( \frac{\partial \bar{u}_i \bar{\omega}_i}{\partial x_j} \frac{\partial \bar{\omega}_i}{\partial x_j} - \frac{\partial \bar{u}_i}{\partial x_j} \frac{\partial \bar{\omega}_i}{\partial x_j} \right). \end{aligned} \quad (26)$$

In Eq. (25),  $-\tau_{ij} \bar{R}_{ij}$  is the production term, which is the helicity transport between the resolved scale and subgrid scale,  $-\frac{1}{\rho} \partial(\bar{p}\bar{\omega}_j - \bar{p}\bar{\omega}_j)/\partial x_j$  is the pressure diffusion term,  $\partial(\bar{u}_j \bar{u}_i \bar{\omega}_i - \bar{u}_j \bar{u}_i \bar{\omega}_i)/\partial x_j$  and  $\frac{1}{2} \partial(\bar{u}_i \bar{u}_i \bar{\omega}_j - \bar{u}_i \bar{u}_i \bar{\omega}_j)/\partial x_j$  are the triple correlation terms, and  $-2\nu(\partial \bar{u}_i / \partial x_j \partial \bar{\omega}_i / \partial x_j - \partial \bar{u}_i / \partial x_j \partial \bar{\omega}_i / \partial x_j)$  is the dissipation term by viscous effects.

The SGS helicity in Eq. (19) can be computed by the transport Eq. (25). In Eq. (26), there are some terms that need to be modeled, including  $\partial(\bar{u}_j \bar{u}_i \bar{\omega}_i - \bar{u}_j \bar{u}_i \bar{\omega}_i)/\partial x_j$ , etc.

#### E. Modeling the h-equation

To obtain insight into the unclosed terms, it is useful to look at the infinite series expansions for each term. For a regular uniform grid ( $dx = dy = dz$ ), Bedford and Yeo<sup>27</sup> derived

$$\begin{aligned} \overline{fg} - \bar{f}\bar{g} &= 2\gamma \frac{\partial \bar{f}}{\partial x_k} \frac{\partial \bar{g}}{\partial x_k} + \frac{1}{2!} (2\gamma)^2 \frac{\partial^2 \bar{f}}{\partial x_k \partial x_l} \frac{\partial^2 \bar{g}}{\partial x_k \partial x_l} \\ &+ \frac{1}{3!} (2\gamma)^3 \frac{\partial^3 \bar{f}}{\partial x_k \partial x_l \partial x_m} \frac{\partial^3 \bar{g}}{\partial x_k \partial x_l \partial x_m} + \dots, \end{aligned} \quad (27)$$

where

$$\gamma(y) = \int_{-\infty}^{\infty} x^2 G(x, y) dx, \quad (28)$$

and  $G(x, y)$  is the kernel of the filter. Considering the isotropic filter,<sup>28</sup> we know that  $\gamma = \Delta^2/24$ . In practical simulation,  $\gamma$  can be taken as  $\gamma = C\Delta^2$ .

For the pressure diffusion term, using the series expansion of Eq. (27) and setting  $f = p$  and  $g = \omega_j$ , one can obtain

$$\frac{1}{\rho} (\overline{p\omega_j} - \bar{p}\bar{\omega}_j) = C_p \Delta^2 \frac{\partial \bar{p}}{\partial x_k} \frac{\partial \bar{\omega}_j}{\partial x_k}. \quad (29)$$

For the triple correlation terms, using Eq. (27) and setting  $f = u_i \omega_i$  and  $g = u_j$ , one can obtain

$$\begin{aligned} \overline{u_i \omega_i u_j} - \bar{u}_i \bar{\omega}_i \bar{u}_j &= 2\alpha \frac{\partial \bar{u}_i \bar{\omega}_i}{\partial x_k} \frac{\partial \bar{u}_j}{\partial x_k} \\ &+ \frac{1}{2!} (2\alpha)^2 \frac{\partial^2 \bar{u}_i \bar{\omega}_i}{\partial x_k \partial x_l} \frac{\partial^2 \bar{u}_j}{\partial x_k \partial x_l} + \dots \end{aligned} \quad (30)$$

Nevertheless,  $u_i \omega_i$  in Eq. (30) cannot be obtained directly in LES, and it needs an approximate form model that can be resolved. As suggested by Pomraning and Rutland,<sup>10</sup> the triple correlation can be approximately estimated as  $2(\bar{\omega}_i \bar{u}_i \bar{u}_j - \bar{\omega}_i \bar{u}_i \bar{u}_j)$ . Then, the series expansion for this model is

$$\begin{aligned} 2(\bar{\omega}_i \bar{u}_i \bar{u}_j - \bar{\omega}_i \bar{u}_i \bar{u}_j) &= 2\bar{\omega}_i (2\alpha) \frac{\partial \bar{u}_i}{\partial x_k} \frac{\partial \bar{u}_j}{\partial x_k} \\ &+ 2\bar{\omega}_i \frac{1}{2!} (2\alpha)^2 \frac{\partial^2 \bar{u}_i}{\partial x_k \partial x_l} \frac{\partial^2 \bar{u}_j}{\partial x_k \partial x_l} + \dots \end{aligned} \quad (31)$$

Thus, the first triple correlation term can be written as

$$-\left( \frac{\partial \bar{u}_i \bar{\omega}_i \bar{u}_j}{\partial x_j} - \frac{\partial \bar{u}_i \bar{\omega}_i \bar{u}_j}{\partial x_j} \right) = -C_{11} \Delta^2 \frac{\partial \bar{\omega}_i}{\partial x_j} \left( \frac{\partial \bar{u}_i}{\partial x_k} \frac{\partial \bar{u}_j}{\partial x_k} \right). \quad (32)$$

As discussed above, the second triple correlation term can be written as

$$\begin{aligned} \frac{1}{2} \frac{\partial (\bar{u}_i \bar{u}_i \bar{\omega}_j - \bar{u}_i \bar{u}_i \bar{\omega}_j)}{\partial x_j} &= \frac{1}{2} \frac{\partial (\bar{u}_i \bar{u}_i \bar{\omega}_j - \bar{u}_i \bar{\omega}_j \bar{u}_i + \bar{u}_i \bar{\omega}_j \bar{u}_i - \bar{u}_i \bar{u}_i \bar{\omega}_j)}{\partial x_j} \\ &= \frac{3}{2} \frac{\partial (\bar{u}_i \bar{\omega}_j \bar{u}_i - \bar{u}_i \bar{u}_i \bar{\omega}_j)}{\partial x_j}, \end{aligned} \quad (33)$$

$$\begin{aligned} \frac{3}{2} (\bar{u}_i \bar{u}_i \bar{\omega}_j - \bar{u}_i \bar{u}_i \bar{\omega}_j) &= \frac{3}{2} \bar{u}_i (2\alpha) \frac{\partial \bar{u}_i}{\partial x_k} \frac{\partial \bar{\omega}_j}{\partial x_k} \\ &+ \frac{3}{2} \bar{u}_i \frac{1}{2!} (2\alpha)^2 \frac{\partial^2 \bar{u}_i}{\partial x_k \partial x_l} \frac{\partial^2 \bar{\omega}_j}{\partial x_k \partial x_l} + \dots \end{aligned} \quad (34)$$

Thus, the second triple correlation term can be written as

$$\frac{1}{2} \frac{\partial (\bar{u}_i \bar{u}_i \bar{\omega}_j - \bar{u}_i \bar{u}_i \bar{\omega}_j)}{\partial x_j} = C_{12} \Delta^2 \frac{\partial \bar{u}_i}{\partial x_j} \left( \frac{\partial \bar{u}_i}{\partial x_k} \frac{\partial \bar{\omega}_j}{\partial x_k} \right). \quad (35)$$

The dissipation term by viscous effects can be modeled as

$$2\nu \left( \frac{\partial \bar{u}_i \bar{\omega}_i}{\partial x_j} \frac{\partial \bar{\omega}_i}{\partial x_j} - \frac{\partial \bar{u}_i}{\partial x_j} \frac{\partial \bar{\omega}_i}{\partial x_j} \right) = C_2 \Delta^2 \frac{\partial \bar{u}_i}{\partial x_k} \frac{\partial \bar{\omega}_i}{\partial x_k}. \quad (36)$$

In the following cases, we give the value of the coefficients as  $C_p = 0.084$ ,  $C_{11} = 0.16$ ,  $C_{12} = 0.078$ , and  $C_2 = 0.17\nu$  based on the DNS results from HIT and turbulent channel flow.

Using the Germano identity, the model can be written as

$$T_{ij} - \frac{1}{3} \delta_{ij} T_{kk} = -2C_{he} \tilde{\Delta}^{3/2} |H|^{1/2} \tilde{S}_{ij}, \quad (37)$$

$$\alpha_{ij} = -2\tilde{\Delta}^{3/2} |H|^{1/2} \tilde{S}_{ij}, \quad (38)$$

$$\beta_{ij} = -2\tilde{\Delta}^{3/2} |h_s|^{1/2} \tilde{S}_{ij}, \quad (39)$$

where

$$H = \widetilde{\bar{u}_i \bar{\omega}_i} - \bar{u}_i \bar{\omega}_i. \quad (40)$$

Using Eqs. (20) and (40), one can obtain

$$H = \tilde{h}_s + \widetilde{\bar{u}_i \bar{\omega}_i} - \bar{u}_i \bar{\omega}_i. \quad (41)$$

The coefficients of the unclosed terms in the equation can also be determined dynamically.

For the pressure diffusion term, one can obtain

$$\frac{\partial \frac{1}{\rho} (\widetilde{\bar{p}\omega_j} - \tilde{p}\tilde{\omega}_j)}{\partial x_j} = -C_p \frac{\partial \frac{1}{\rho} \left( \tilde{\Delta}^2 \frac{\partial \tilde{p}}{\partial x_k} \frac{\partial \tilde{\omega}_j}{\partial x_k} - \Delta^2 \frac{\partial \bar{p}}{\partial x_k} \frac{\partial \bar{\omega}_j}{\partial x_k} \right)}{\partial x_j}. \quad (42)$$

For the first triple term  $(-\partial \bar{u}_i \bar{\omega}_i \bar{u}_j / \partial x_j - \partial \bar{u}_i \bar{\omega}_i \bar{u}_j / \partial x_j) \approx -2(\partial (\bar{\omega}_i \bar{u}_i \bar{u}_j - \bar{\omega}_i \bar{u}_i \bar{u}_j) / \partial x_j)$ , one can obtain

$$2 \frac{\partial \bar{\omega}_i (\widetilde{\bar{u}_i \bar{u}_j} - \bar{u}_i \bar{u}_j)}{\partial x_j} = -C_{11} \frac{\partial \bar{\omega}_i \left( \tilde{\Delta}^2 \left( \frac{\partial \tilde{u}_i}{\partial x_k} \frac{\partial \tilde{u}_j}{\partial x_k} \right) - \Delta^2 \left( \frac{\partial \bar{u}_i}{\partial x_k} \frac{\partial \bar{u}_j}{\partial x_k} \right) \right)}{\partial x_j}. \quad (43)$$

For the second triple term  $(\frac{1}{2} \partial (\bar{u}_i \bar{u}_i \bar{\omega}_j - \bar{u}_i \bar{u}_i \bar{\omega}_j) / \partial x_j) \approx \frac{3}{2} \partial (\bar{u}_i \bar{\omega}_j \bar{u}_i - \bar{u}_i \bar{u}_i \bar{\omega}_j) / \partial x_j$ , one can obtain

$$\frac{3}{2} \frac{\partial \bar{u}_i (\widetilde{\bar{u}_i \bar{\omega}_j} - \bar{u}_i \bar{\omega}_j)}{\partial x_j} = -C_{12} \frac{\partial \bar{u}_i \left( \tilde{\Delta}^2 \left( \frac{\partial \tilde{u}_i}{\partial x_k} \frac{\partial \tilde{\omega}_j}{\partial x_k} \right) - \Delta^2 \left( \frac{\partial \bar{u}_i}{\partial x_k} \frac{\partial \bar{\omega}_j}{\partial x_k} \right) \right)}{\partial x_j}. \quad (44)$$

For the dissipation term by viscous effects, one can obtain

$$2\nu \left( \frac{\partial \widetilde{\bar{u}_i \bar{\omega}_i}}{\partial x_j} \frac{\partial \tilde{\omega}_i}{\partial x_j} - \frac{\partial \bar{u}_i}{\partial x_j} \frac{\partial \bar{\omega}_i}{\partial x_j} \right) = -C_2 \left( \tilde{\Delta}^2 \frac{\partial \bar{u}_i}{\partial x_k} \frac{\partial \bar{\omega}_i}{\partial x_k} - \Delta^2 \frac{\partial \bar{u}_i}{\partial x_k} \frac{\partial \bar{\omega}_i}{\partial x_k} \right). \quad (45)$$

Then, we will discuss the realizability of the  $h$ -equation model here. Schumann<sup>29</sup> has shown that to guarantee a realizable solution

for a subgrid-scale stress tensor, the following conditions should be considered:

$$\tau_{ij} \geq 0 \quad (\text{for } i = j), \quad (46)$$

$$\tau_{[ij]}^2 \leq \tau_{[ij]}\tau_{[ij]} \quad (\text{for } i \neq j), \quad (47)$$

$$\det(\tau_{ij}) \geq 0. \quad (48)$$

One can find that the SGS helicity one-equation model satisfies the realizability conditions according to the DNS case.

### III. NUMERICAL RESULTS AND ANALYSIS

#### A. Homogeneous and isotropic turbulence

The SGS helicity one-equation model is first tested to assess *a priori* the incompressible homogeneous and isotropic turbulence.

The full Navier–Stokes equations and the filtered Navier–Stokes equations are solved using a pseudo-spectral model in a cubic domain with the side length  $L = 2\pi$ . Periodic boundary conditions are employed in the three coordinate directions. The phase-shift method together with the  $\sqrt{2}/3$  rule is applied to remove the dealiasing error. The second-order Adams–Bathforth scheme is applied to integrate the governing equations<sup>21</sup> temporally.

The turbulent field is initially generated by a Gaussian random field as

$$E_0(k) = Ak^2 U_0^2 k_0^{-5} e^{-2k^2/k_0^2}, \quad (49)$$

with  $k_0 = 4.5786$  and  $U_0 = 0.715$ , and the constant  $A$  can be determined when the initial kinetic energy is equal to  $3U_0^2/2$ . The whole system is maintained by constant energy and helicity injection rates ( $\varepsilon = 0.1$  and  $\eta = 0.3$ ) in the first two wavenumber shells.<sup>21</sup> The grid resolution for DNS is  $1024 \times 1024 \times 1024$  and that for LES is  $64 \times 64 \times 64$ . The Taylor Reynolds number ( $Re_\lambda$ ) for DNS is 341. According to K41,<sup>30</sup> the viscous effect can be ignored in the inertial subrange, and the SGS energy and helicity dissipations are unchanged with the changed filter width, which ensures the scale invariance of the SGS model in LES.

Figures 1(a) and 1(b) show the SGS energy and helicity dissipations vs the normalized filter width  $\delta/\zeta$  from the *a priori* test of different models ( $\delta$  is the filter width, and  $\zeta$  is the Kolmogorov scale). The SGS dissipations calculated by the real SGS stress tensor are also presented as a reference for comparison. The trends of the SGS dissipations predicted by both the *h*-equation and SM models are close to constant in the inertial subrange ( $60 < \delta/\zeta < 120$ ), which is similar to the results calculated by the real SGS stress. Additionally, we can find that the values predicted by the SM are higher than those of the real SGS stress and the *h*-equation model, which are closer to the real results. The DSM has the worst behavior. Tables I and II show the percentage errors from different models in Figs. 1(a) and 1(b). The percentage errors of the *h*-equation model are less than that of SM.

Furthermore, through the *a priori* results, we could infer that the *h*-equation model could also provide better prediction results in the *a posteriori* test.

Figure 2 shows the energy spectrum and helical spectrum in the system driven by constant injection rates of energy and helicity, i.e.,  $\varepsilon = 0.1$  and  $\eta = 0.3$ . From Figs. 2(a) and 2(b), the *h*-equation model and the dynamic *h*-equation model (*dh*-equation) can well predict the spectra of energy and helicity, which are slightly better than those of

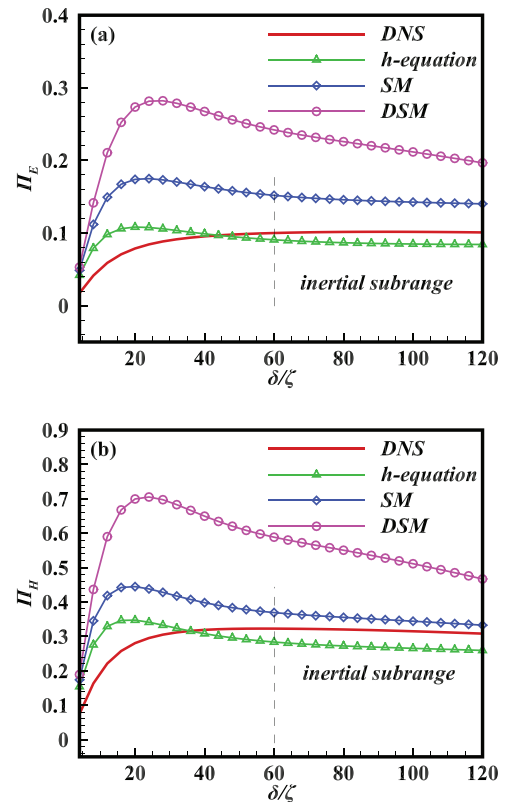


**FIG. 1.** The SGS energy dissipation ( $\Pi_E$ ) and SGS helicity dissipation ( $\Pi_H$ ) in the system are driven by constant injection rates of energy and helicity, i.e.,  $\varepsilon = 0.1$  and  $\eta = 0.3$ ; (a) the SGS energy dissipation ( $\Pi_E$ ) and (b) the SGS helicity dissipation ( $\Pi_H$ ).

the DSM and the *dh*-equation model. As Figs. 2(a) and 2(b) show, because the SGS dissipations predicted by the *h*-equation model are lower than those predicted by the SM model, the *dh*-equation model predicts the energy spectrum to be slightly lower than that of the DSM at  $3 < k < 9$  and predicts the energy spectrum to be slightly higher than that of the DSM at  $10 < k < 12$ . Tables III and IV list the percentage error from different models in Figs. 2(a) and 2(b).

In addition, the validity check of the *h*-equation in the turbulence with chiral symmetry is provided here. We employ the new model in

**TABLE I.** The percentage errors of the energy dissipation compared to DNS from different models against different  $\delta/\zeta$  in Fig. 1(a).

$\delta/\zeta$	h	SM
10	77%	160%
20	27%	120%
30	16%	91%
50	−4%	59%
70	−12.5%	47%
90	−15.8%	41.5%
110	−16.6%	39%

**TABLE II.** The percentage errors of the helicity dissipation compared to DNS from different models against different  $\delta/\zeta$  in Fig. 1(b).

$\delta/\zeta$	h	SM
10	57%	98.9%
20	23%	58%
30	6.4%	37%
50	-8.9%	18%
70	-13.9%	12.3%
90	-15.5%	10%
110	-10%	8%

the system are driven by constant injection rates of energy and helicity, i.e.,  $\varepsilon = 0.1$  and  $\eta = 0.0$ . The Taylor Reynolds number ( $Re_\tau$ ) for DNS is 306. The grid resolution for DNS is also  $1024 \times 1024 \times 1024$  and that for LES is  $64 \times 64 \times 64$ .

Figure 3 shows the energy spectrum in the system driven by only a constant injection rate of energy, i.e.,  $\varepsilon = 0.1$  and  $\eta = 0.0$ . The  $dh$ -equation model can perfectly predict the energy spectrum, and the  $h$ -equation model also performs better than the DSM, the SM, the  $k$ -equation model, and the  $dk$ -equation model. From the results above,

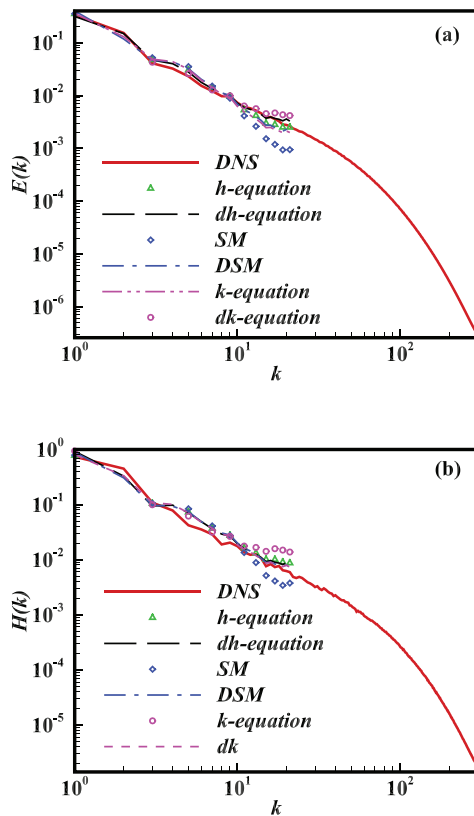


**FIG. 2.** The energy spectrum and helicity spectrum in the system driven by constant injection rates of energy and helicity, i.e.,  $\varepsilon = 0.1$  and  $\eta = 0.3$ ; (a) the energy spectrum and (b) the helicity spectrum.

**TABLE III.** The percentage errors of the energy spectrum compared to DNS from different models against different  $\delta/\zeta$  in Fig. 2(a).

$\delta/\zeta$	h	SM	k	dh	DSM	dk
2	-12.9%	-13.2%	-15.3%	-2.7%	-23%	-24.9%
4	30.2%	51.7%	35.1%	23.6%	34.9%	12.4%
6	22.6%	38.9%	27.8%	16%	32.3%	8%
10	-8.7%	-23%	-15%	-1.8%	-6.4%	1.3%
14	-21.7%	-55.3%	-33.67%	-4.4%	-26.3%	13%
18	-17.5%	-67.7%	-34.3%	8.9%	-28.6%	41%
21	-5.5%	-64.3%	-24.6%	23.9%	-20.9%	57.8%

**TABLE IV.** The percentage errors of the helical spectrum compared to DNS from different models against different  $\delta/\zeta$  in Fig. 2(b).

$\delta/\zeta$	h	SM	k	dh	DSM	dk
2	-20%	-24%	-32%	-26%	-31.8%	-26%
4	14.5%	40.7%	3.8%	24.9%	19.4%	28.8%
6	27.9%	56%	12%	38%	38%	38%
10	10.2%	0.3%	13.7%	11.3%	14.6%	7%
14	11.5%	-34.9%	52%	3.4%	2%	-4%
18	28%	-51%	-100%	10%	-6%	8%
21	46%	-37%	130%	25%	22%	23%

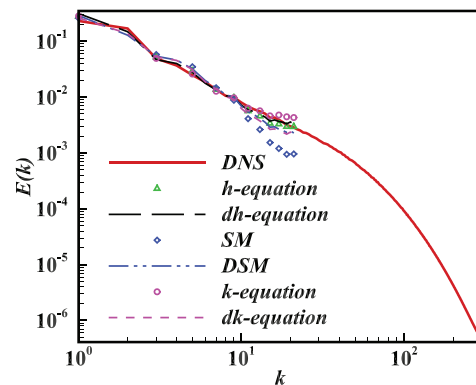


**FIG. 3.** The energy spectrum and helicity spectrum in the system driven by constant injection rates of energy and helicity, i.e.,  $\varepsilon = 0.1$  and  $\eta = 0.0$ .

we can infer that the  $h$ -equation model is a common SGS model for the large-eddy simulation of 3D turbulent flows. Table V lists the percentage error from different models in Fig. 3.

**B. Turbulent channel flow**

The  $h$ -equation model is also tested and assessed *a posteriori* in turbulent channel flow. The Fourier–Chebyshev pseudo-spectral algorithm method is applied to solve the governing equations.<sup>31</sup> The second-order Adams–Bashforth scheme is applied for the nonlinear term for temporal integration. The dealiasing error is removed by the phase-shift method together with the 2/3 rule.<sup>32</sup> Periodic boundary

**TABLE V.** The percentage errors of the energy spectrum compared to DNS from different models against different  $\delta/\zeta$  in Fig. 3.

$\delta/\zeta$	h	SM	k	dh	DSM	dk
2	-21.5%	-20%	-24%	-12%	-24%	-18%
4	16%	39%	5%	12%	25%	23%
6	-2%	11.9%	-11.5%	-4%	6%	2%
10	-14%	-31%	-8%	-10%	-14%	22%
14	-20%	-59%	-4%	-13%	-30%	-36%
18	-11%	-69%	-31%	0.7%	-29%	34%
21	3.5%	-66%	51%	10%	-20%	-23%

conditions are supplied in the streamwise (x) and spanwise (z) directions and non-slip boundary conditions are designated at walls ( $y = \pm\delta$ ), where  $\delta$  is the channel half-width. This channel flow is driven by a constant pressure gradient along the streamwise direction. The grid filter width is set as  $\Delta = [\Delta_x\Delta_y(y)\Delta_z]^{1/3}$ , where  $\Delta_x$ ,  $\Delta_y(y)$  and  $\Delta_z$  are the local grid spacings. In this paper, the top-hat filter is adopted by integrating over space points using Simpson's rule.<sup>33</sup> For the dynamic procedure, the subtest filter is set to be  $2\Delta$  correspondingly. For the sake of analysis, we select six SGS models for comparison: the *h*-equation model, the *dh*-equation model, the *k*-equation model, the *dk*-equation model, the SM, and the DSM. For constant-coefficient models, we use the van Driest damping function near the wall.<sup>34</sup>

As suggested by Moser and Mansour,<sup>35</sup> the computational domain is a three-dimensional box of size  $2\pi h \times 2h \times \pi h$  ( $h$  is the half-width of the channel) with  $256 \times 192 \times 192$  at  $Re_\tau = 395$ , and another computational domain is  $4\pi h \times 2h \times 2\pi h$  with  $192 \times 193 \times 192$  at  $Re_\tau = 180$ . The DNS results are in good agreement with the data from Moser and Mansour.<sup>35</sup> For the LES model, the coarser the grid is, the more challenging the modeling is, and the more convincing model quality that is perceived.<sup>36</sup> From Meyers's discussion, the grid resolution of the large-eddy simulation is chosen as  $48 \times 48 \times 48$  at  $Re_\tau = 180$  and  $48 \times 64 \times 48$  at  $Re_\tau = 395$ . The grid resolution that we choose is slightly coarser than that chosen previously.<sup>37</sup>

The details of the parameter settings are listed in Tables VI and VII (case 1 is at  $Re_\tau = 180$ , and case 2 is at  $Re_\tau = 395$ ).

Figure 4 shows the SGS energy dissipation ( $\Pi_E$ ) at  $Re_\tau = 395$  from *a priori*. The *dh*-equation and the *dk*-equation models can have better performance than the DSM. The *dk*-equation model predicts the SGS energy dissipation lower than the real values.

Figures 5(a) and 5(b) show the normalized mean velocity ( $U^+ = \langle \bar{u} \rangle / u_\tau$ ) profiles from different models at  $Re_\tau = 180$  and  $Re_\tau = 395$ , respectively. In the two cases, the simulation results of these models display a similar trend. As Fig. 5 shows, the *dh*-equation model gives perfect predictions of the velocity profiles compared with

**TABLE VI.** Parameters of the simulations in channel flow for DNS.

Case	Grids	$\Delta x^+$	$\Delta y_{min}^+$	$\Delta z^+$
Case1	$192 \times 193 \times 192$	11.78	0.024	5.88
Case2	$256 \times 192 \times 192$	9.68	0.053	6.45

**TABLE VII.** Parameters of the simulations in channel flow for LES.

Case	Grids	$\Delta x^+$	$\Delta y_{min}^+$	$\Delta z^+$
Case1	$48 \times 48 \times 48$	47.12	0.38	23.56
Case2	$48 \times 64 \times 48$	51.68	0.48	25.84

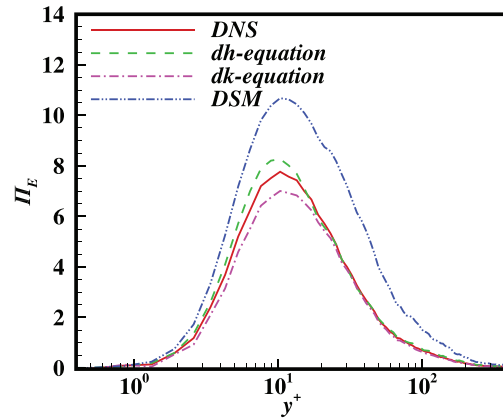


**FIG. 4.** The SGS energy dissipation ( $\Pi_E$ ) under  $\Delta_z$  filter width at  $Re_\tau = 395$ .

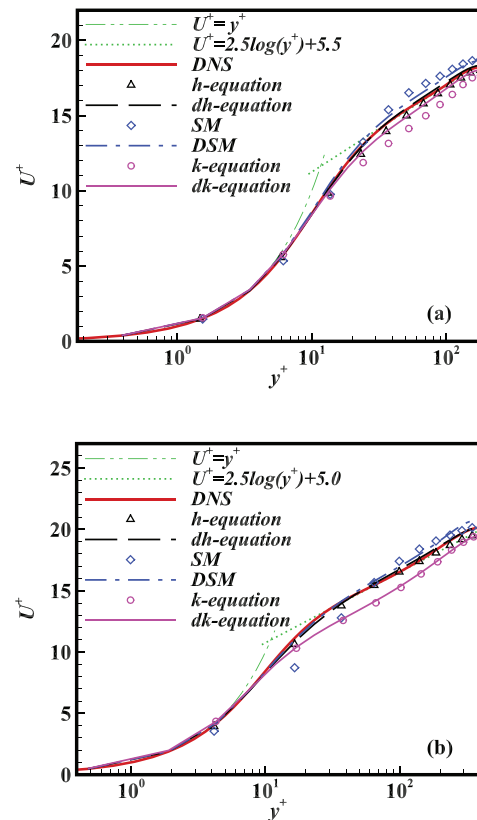


**FIG. 5.** The mean velocity profiles in the wall unit at (a)  $Re_\tau = 180$  and (b)  $Re_\tau = 395$ .



**TABLE VIII.** The percentage errors of the mean velocity profiles compared to DNS from different models against different  $y^+$  in Fig. 5(a).

$y^+$	h	SM	k	dh	DSM	dk
10	-1.5%	7%	-4%	-0.5%	1.6%	-0.9%
20	-3.6%	-1.2%	-8.7%	-0.5%	2%	-3.3%
30	-3.6%	3.9%	-9.6%	0.12%	2.5%	-3.5%
50	-2.7%	6.5%	-9%	0.5%	2.7%	-3.2%
80	-1.5%	5.4%	-6.7%	1%	3%	-2%
100	-1%	4.7%	-5.8%	1%	3%	-1.5%
150	-1.17%	3%	-3.5%	0.6%	2.5%	-1.2%

the DNS profiles at both  $Re_\tau = 180$  and  $395$  and agrees well with the log-law line in the logarithmic region. Tables VIII and IX list the percentage error from different models in Figs. 5(a) and 5(b).

The profiles of the  $h$ -equation model and the DSM are also close to the real profile and apparently better than that of the SM. The only difference between the results of the  $h$ -equation and the DSM is that the mean velocity profile predicted by the  $h$ -equation model is slightly lower than that of the DNS, and the results from the DSM are slightly higher than those from DNS. The  $dk$ -equation model can obtain good results at a low Reynolds number. The  $k$ -equation model and  $dk$ -equation model well predict the mean velocity profiles in the near-wall region, but worse in the log-law region than DSM because of the lower SGS energy dissipation.

For steady-state turbulent channel flow, there is a balance equation for the total shear stress along the wall-normal direction, and the total shear stress  $\tau_{tot}$  is composed of two important parts, which include the viscous stress  $\tau_\mu$  and the Reynolds shear stress  $R_{uv}$ <sup>28</sup>

$$\tau_{tot} = \tau_\mu + R_{uv}. \tag{50}$$

The viscous stress  $\tau_\mu$  is dominant in the viscous sublayer. Shown in Fig. 6 is the normalized resolved viscous shear stress ( $\tau_\mu/\tau_w$ ) from different models at  $Re_\tau = 180$  and  $Re_\tau = 395$ , and the real value from DNS is also displayed here for comparison. As Fig. 6 shows, the  $dh$ -equation model still perfectly predicts the viscous shear stress. The  $h$ -equation model, the DSM, the  $k$ -equation model, and the  $dk$ -equation model also perform better than the profiles from the SM. Tables X and XI list the percentage error from different models in Figs. 6(a) and 6(b).

**TABLE IX.** The percentage errors of the mean velocity profiles compared to DNS from different models against different  $y^+$  in Fig. 5(b).

$y^+$	h	SM	k	dh	DSM	dk
10	-4%	-22%	-2.8%	-1.8%	-0.7%	-2.8%
20	-4.5%	-19.6%	-9%	-3%	-1.5%	-9%
50	-0.8%	-3%	-10.7%	-0.1%	1.4%	9%
80	0.1%	4%	-9%	0.1%	2.5%	-8%
200	-1.5%	3.5%	-5.5%	0.6%	2.9%	-5.1%
300	-2.5%	1%	-4%	0.1%	3.4%	-4%
390	-2.8%	0.3%	-3%	0.1%	3.3%	-3.1%

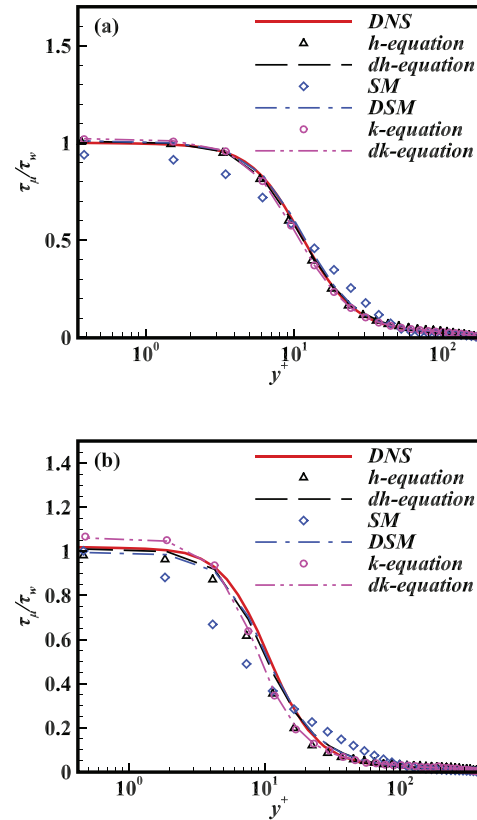


**FIG. 6.** The normalized viscous shear stress distribution against  $y^+$  from different models (a) at  $Re_\tau = 180$  and (b) at  $Re_\tau = 395$ .

The Reynolds shear stress  $R_{uv}(-\langle uv \rangle)$  plays a dominant role in the log-law region. In LES, it is composed of two parts, which are the resolved and modeled stress. In Fig. 7, we present the results of the normalized Reynolds shear stress ( $R_{uv}/\tau_w$ ) from different models in the two cases, and the DNS result is supplied for comparison. As shown in Fig. 7, we find that the three dynamic models can generally perform well, but the DSM result deviates from the real value in the centerline region of the high Reynolds number case ( $Re_\tau = 395$ ). The  $dk$ -equation model result is a lot higher than that of DNS. For the constant-coefficient models, the result of the  $h$ -equation model

**TABLE X.** The percentage errors of the normalized viscous shear stress compared to DNS from different models against different  $y^+$  in Fig. 6(a).

$y^+$	h	SM	k	dh	DSM	dk
1	0.1%	7%	1.5%	0.5%	0.7%	1.8%
5	-3.8%	-14%	-3.2%	-2.2%	-0.6%	-2.8%
10	-6.6%	-3.4%	-6.8%	-1.5%	2.6%	-6.5%
20	-5.8%	42%	-6.5%	3.4%	6.2%	-6.4%
40	9%	44%	2%	13%	7%	3%
150	9%	-14%	33%	14%	15%	26%

**TABLE XI.** The percentage errors of the normalized viscous shear stress compared to DNS from different models against different  $y^+$  in Fig. 6(b).

$y^+$	h	SM	k	dh	DSM	dk
1	-4%	-8%	4%	-0.9%	2.5%	3.8%
5	-11%	-37%	-3.5%	-3%	-4%	-3.6%
10	-23%	-28%	-19%	-6%	-4%	-17%
20	-28%	20%	-23%	4%	6%	-21%
50	18%	140%	10%	30%	31%	16%
100	19%	27%	16%	3.6%	3%	14.6%
200	71%	-17%	87%	20%	42%	51%

perfectly approaches the real value in the low Reynolds number case ( $Re_\tau = 180$ ), but in the buffer layer and log-law region of the high Reynolds number case, the  $h$ -equation model weakens the Reynolds shear stress. The  $k$ -equation model performs a lot worse than the  $h$ -equation model. In both cases, the SM cannot reasonably predict the Reynolds shear stress. Tables XII and XIII list the percentage error from different models in Figs. 7(a) and 7(b). The percentage errors of the  $h$ -equation and  $dh$ -equation model are less than that of DSM in the log-law region from the tables.

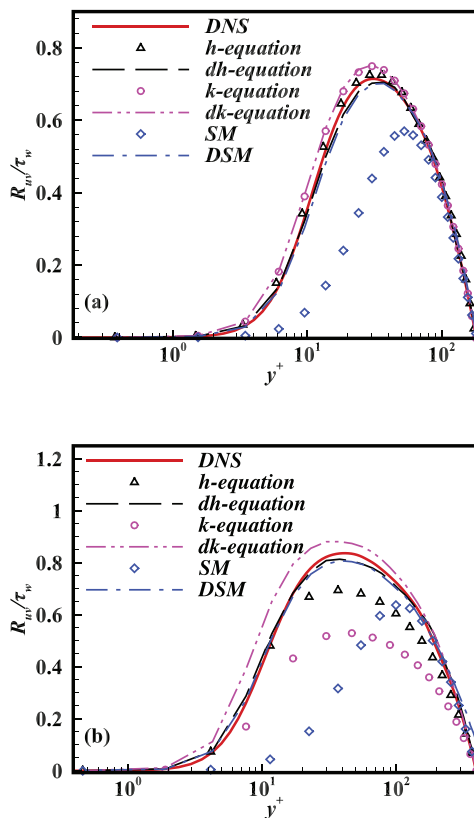


**FIG. 7.** The resolved Reynolds stress normalized by friction velocity  $u_\tau$  vs  $y^+$  from different models (a) at  $Re_\tau = 180$  and (b) at  $Re_\tau = 395$ .

**TABLE XII.** The percentage errors of the resolved Reynolds stress compared to DNS from different models against different  $y^+$  in Fig. 7(a).

$y^+$	h	SM	k	dh	DSM	dk
5	50%	-80%	63%	20%	15%	64%
10	8.8%	-78%	16%	-3%	-8%	17%
20	1.7%	-59%	5%	-4%	-5%	7%
50	2%	-15%	3%	0.4%	-0.5%	2.5%
100	1.5%	-7%	6.9%	4.6%	3%	2.6%
150	9.8%	-8%	2.5%	2%	11%	6.8%

We show in Figs. 8–10 the resolved turbulence intensities [ $\bar{u}_i^{rms} = \langle (\bar{u}_i - \langle \bar{u}_i \rangle)^2 \rangle^{1/2}$ ] calculated from the  $h$ -equation model, the  $dh$ -equation model, the SM, the DSM, the  $k$ -equation model, and the  $dk$ -equation model at  $Re_\tau = 180$  and  $Re_\tau = 395$ . Figures 8(a), 9(a), and 10(a) show the streamwise, wall-normal, and spanwise turbulence intensity distributions against  $y^+$  at  $Re_\tau = 180$ , respectively, and the DNS data are also presented for comparison purposes.

For  $Re_\tau = 180$ , it is visually apparent that the resolved turbulence intensities given by the  $h$ -equation are closest to the DNS data in almost all the regions. The  $k$ -equation model predicts the results a lot lower than the  $h$ -equation model at  $0 < y^+ < 50$  in Fig. 8(a). The performance of the  $dh$ -equation is slightly better than that of the DSM and the  $dk$ -equation model, while the performance of the SM is relatively poor compared with that of other models.

The resolved turbulence intensities for  $Re_\tau = 395$  are supplied in Figs. 8(b), 9(b), and 10(b). In this case, the  $dh$ -equation model behaves best except for a slight drop in predicting the normal-wall and spanwise components in part of the buffer layer and log-law region ( $20 < y^+ < 150$ ). It shows that the proposed model based on SGS helicity can better capture the turbulent fluctuations, and the reason may be the  $dh$ -equation model could supply more proper SGS energy dissipations according to the *a priori* test than other models. The DSM, the  $h$ -equation model, the  $k$ -equation model, and the  $dk$ -equation model can also give acceptable results. The SM can't capture the turbulent fluctuations in the full region. The turbulence intensities predicted by the  $k$ -equation and  $dk$ -equation model are higher than real values except for the spanwise turbulence intensity at  $Re_\tau = 395$  because the averaged SGS energy dissipations predicted by the  $dk$ -equation are lower than real values. Tables XIV and XV list the percentage error from different models in Figs. 8(a) and 8(b). Tables XVI and XVII list the percentage error from different models in Figs. 9(a) and 9(b).

**TABLE XIII.** The percentage errors of the resolved Reynolds stress compared to DNS from different models against different  $y^+$  in Fig. 7(b).

$y^+$	h	SM	k	dh	DSM	dk
5	29%	-92%	-26%	26%	21%	77%
10	2%	-91%	-34%	7%	3.4%	35.8%
30	-15.8%	-70%	-37%	-1.6%	-3.4%	7%
100	-16.6%	-11%	-35%	-2%	-3%	4%
200	-12%	-0.4%	31%	6%	3%	7%
300	-13%	-0.2%	-32%	8%	21%	3.5%

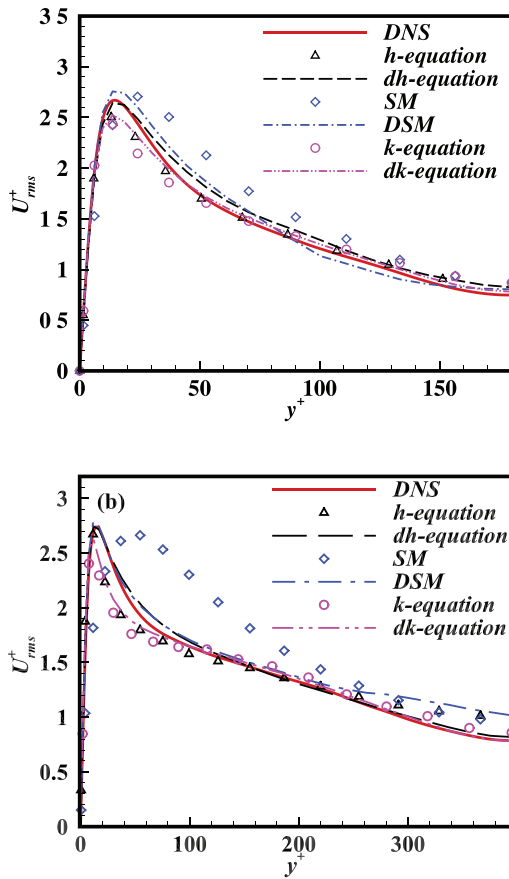


FIG. 8. Profiles of turbulence intensities (a)  $U_{rms}^+$ , at  $Re_\tau = 180$  and (b)  $U_{rms}^+$ , at  $Re_\tau = 395$ .

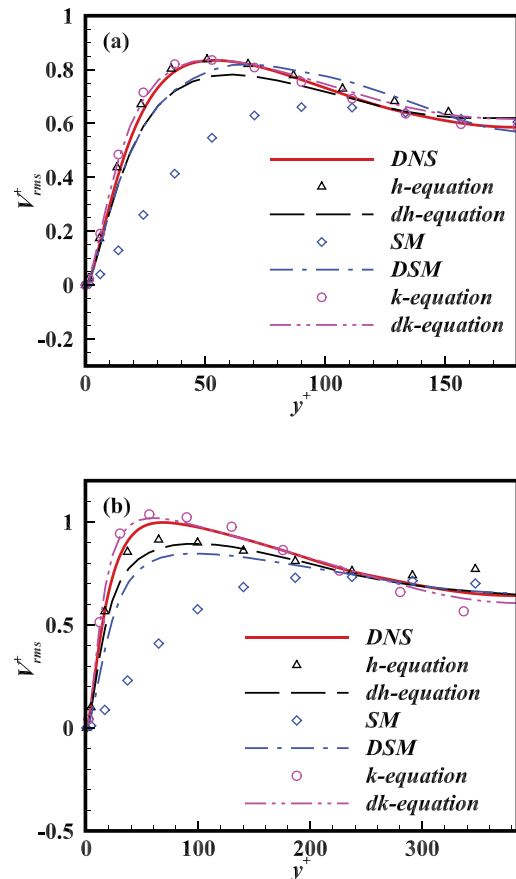


FIG. 9. Profiles of turbulence intensities (a)  $V_{rms}^+$ , at  $Re_\tau = 180$  and (b)  $V_{rms}^+$ , at  $Re_\tau = 395$ .

Tables XVIII and XIX list the percentage error from different models in Figs. 10(a) and 10(b). Table XX lists the time to compute LES every 20 time steps with 24 CPU.

The coherent structure is one of the main characteristics of turbulent flows, and the ability of coherent-structure capture is an important evaluation criterion of LES. The second invariant of the strain rate tensor  $Q$  is a method of vortex structure identification<sup>38</sup>

$$Q = -1/2(S_{ij}S_{ij} - W_{ij}W_{ij}), \quad (51)$$

where

$$S_{ij} = \frac{1}{2} \left( \frac{\partial u_i}{\partial x_j} + \frac{\partial u_j}{\partial x_i} \right), \quad W_{ij} = \frac{1}{2} \left( \frac{\partial u_i}{\partial x_j} - \frac{\partial u_j}{\partial x_i} \right). \quad (52)$$

Figures 11 and 12 show the instantaneous isosurfaces of different  $Q$  at  $Re_\tau = 395$ . From the figures, we can find that the  $dh$ -equation can identify abundant vortex structures, and the  $dh$ -equation model result is most similar to the result from DNS. The DSM and the  $dk$ -equation model can also capture abundant vortex structures, and they are mainly concentrated near the wall region. In the near-wall region, many vortex structures are caught by the  $h$ -equation and the  $k$ -equation, and they

also have a small amount of distribution in the centerline region. In contrast, the SM can only capture some large-scale vortices. The  $h$ -equation model behaves a little better than the  $k$ -equation model. Hence, based on the  $Q$  analysis, we could infer that the  $dh$ -equation model and the  $h$ -equation model have the intrinsic advantage of capturing the vortex structure for modeling through the SGS helicity.

#### IV. CONCLUSION AND DISCUSSION

In this paper, we choose subgrid-scale helicity as the target physical quantity to construct a new subgrid-scale model for large-eddy simulation of turbulent flows. The SGS helicity reflects the helicity transfer between the resolved scale and subgrid scale. First, a relationship between the SGS helicity and SGS viscosity is established through the theoretical derivation in the spectral space of homogeneous and isotropic helical turbulence. Then, we obtain the SGS helicity transport equation from the Navier–Stokes equations. For the unclosed terms of the SGS helicity equation, we use the infinite series expansions method to model each one of them.

The new models ( $h$ -equation model and  $dh$ -equation model) initially use *a priori* and *a posteriori* tests in homogenous and isotropic helical turbulence. These tests have proven the reasonability in modeling and excellent character in predicting turbulence compared with

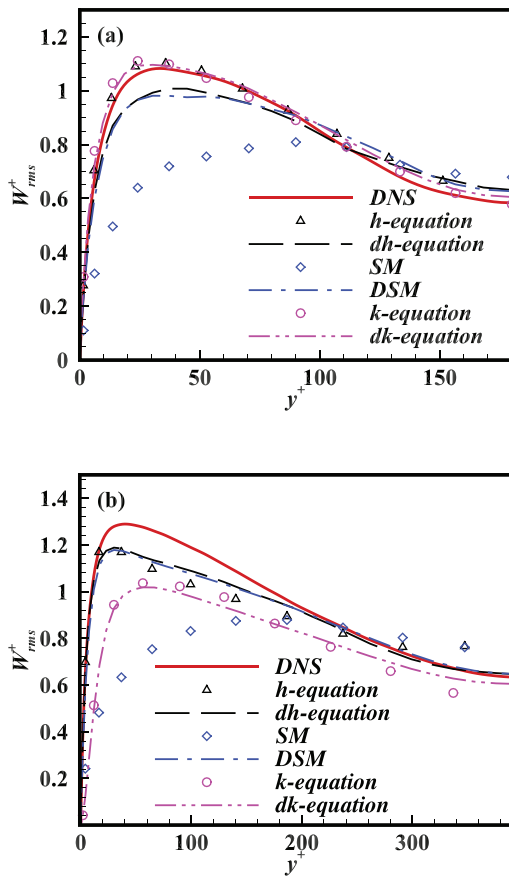


FIG. 10. Profiles of turbulence intensities (a)  $W_{rms}^+$  at  $Re_\tau = 180$  and (b)  $W_{rms}^+$  at  $Re_\tau = 395$ .

TABLE XIV. The percentage errors of the streamwise turbulence intensities compared to DNS from different models against different  $y^+$  in Fig. 8(a).

$y^+$	h	SM	k	dh	DSM	dk
10	-5%	-17%	-4%	-2.5%	-2%	-4%
20	-7%	3%	-12%	0.5%	5%	-6%
50	-1.6%	26%	-3%	7%	10%	1%
80	1.7%	18%	2%	6.7%	3%	3%
120	3.4%	14%	7%	4%	-6%	3%
170	11%	17%	16%	11%	7%	5%

other classic SGS models. Furthermore, we have verified the universality of the model for non-helical turbulence. In turbulent channel flow for various Reynolds numbers, the  $h$ -equation model and the dynamic  $h$ -equation model are also tested for their validity. The DSM, the SM, the  $k$ -equation model, and the  $dk$ -equation model are compared. From the simulation results, we find that the  $h$ -equation model and  $dh$ -equation model can obtain more accurate mean turbulence fields at various Reynolds number flows, such as the mean velocity profiles,

TABLE XV. The percentage errors of the streamwise turbulence intensities compared to DNS from different models against different  $y^+$  in Fig. 8(b).

$y^+$	h	SM	k	dh	DSM	dk
10	1.7%	-34%	5.8%	0.6%	2.8%	-0.5%
60	-6%	40%	-10%	5%	5%	-4%
120	-2.6%	34%	2%	1.8%	3%	1.4%
200	-0.4%	16%	5.8%	-1.5%	3%	2%
300	11%	14%	7%	2%	20%	2%
380	27%	22%	8%	4%	31%	-0.2%

TABLE XVI. The percentage errors of the wall-normal turbulence intensities compared to DNS from different models against different  $y^+$  in Fig. 9(a).

$y^+$	h	SM	k	dh	DSM	dk
10	12%	-71%	20%	-8%	-8%	16%
20	6.8%	-63%	12.8%	-9%	-10%	8%
50	0.5%	-37%	0.3%	-7%	-5%	0.2%
80	0.3%	-17%	-1%	-4%	2%	0.5%
120	4%	-3%	-0.4%	-0.1%	8%	3%
150	5%	2%	-0.7%	2%	4%	4%

TABLE XVII. The percentage errors of the wall-normal turbulence intensities compared to DNS from different models against different  $y^+$  in Fig. 9(b).

$y^+$	h	SM	k	dh	DSM	dk
20	-2%	-83%	19%	-16%	-31%	15%
60	-8%	-61%	4%	-13%	-18%	2.5%
120	-7%	-32%	5%	-6%	-11%	0.1%
200	-2.8%	-10%	-0.6%	-2%	-5%	0.4%
300	8%	3%	-9%	-0.2%	0.1%	-3%
380	22%	8%	-16%	1%	2%	-5%

TABLE XVIII. The percentage errors of the spanwise turbulence intensities compared to DNS from different models against different  $y^+$  in Fig. 10(a).

$y^+$	h	SM	k	dh	DSM	dk
10	4%	-50%	11%	-7%	-10%	6%
20	2.8%	-43%	5%	-6%	-9%	3.4%
40	1.8%	-32%	1%	-6%	-9%	1%
100	2%	-5%	-0.9%	-1%	3%	2.6%
130	7%	5.8%	2.5%	4.6%	8%	4.7%
160	-6%	13.8%	0.8%	8%	6.7%	3.4%

the viscous shear stress, and the Reynolds shear stress. The percentage errors tables can also be referenced to prove above. However, the new models still have no apparent advantages over  $k$ -equation and  $dk$ -equation models in predicting turbulent stress. As the results of the *a priori* test in HIHT show that the  $h$ -equation model can supply a more

**TABLE XIX.** The percentage errors of the spanwise turbulence intensities compared to DNS from different models against different  $y^+$  in Fig. 10(b).

$y^+$	h	SM	k	dh	DSM	dk
20	-3%	-58%	-36%	-5%	-6%	-38%
60	-12.8%	-42%	-18.5%	-10%	-10.6%	-20%
120	-12.3%	-25%	-12.8%	-7%	-8%	-16.9%
200	-6%	-6%	-12.5%	-1.8%	-1.6%	-11.6%
300	5%	10%	-13%	-2%	1%	-7.6%
380	21%	18%	-16%	2%	2%	-5%

**TABLE XX.** The time to compute LES every 20 time steps with 24 CPU.

$y^+$	SM	h	DSM	dh
Time	1.2 s	2 s	3 s	4 s

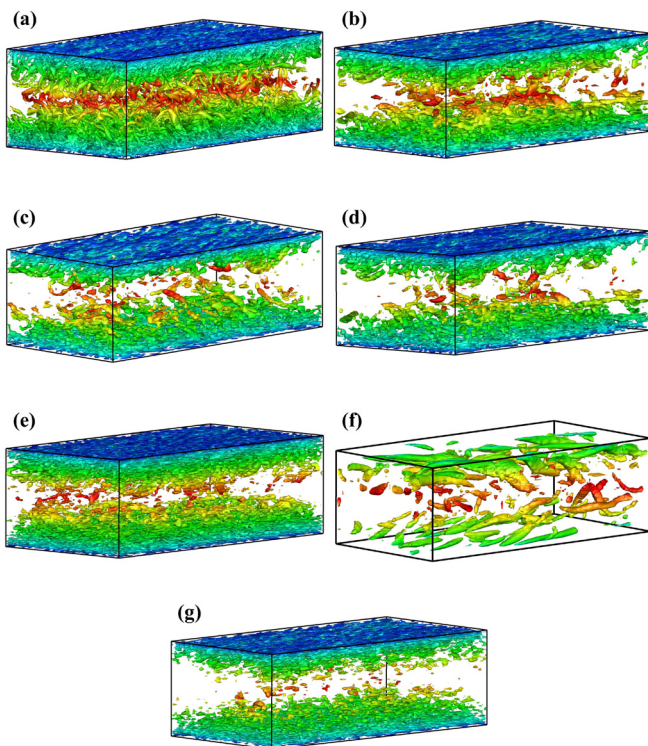


**FIG. 11.** Instantaneous isosurface of  $Q = 250$  obtained from different models in turbulent channel flow of the  $Re_\tau = 395$  (a) DNS, (b)  $dh$ -equation model, (c) DSM, (d)  $dk$ -equation model, (e)  $h$ -equation model, (f) SM, and (g)  $k$ -equation model.

accurate SGS dissipation than the SM, we infer that the proper SGS dissipation furnished by the  $h$ -equation model and the  $dh$ -equation model is the radical guarantee for the models to predict the proper mean turbulence fields. The new proposed models can also capture finer vortex structures ( $Q$  analysis) in turbulent channel flow. As

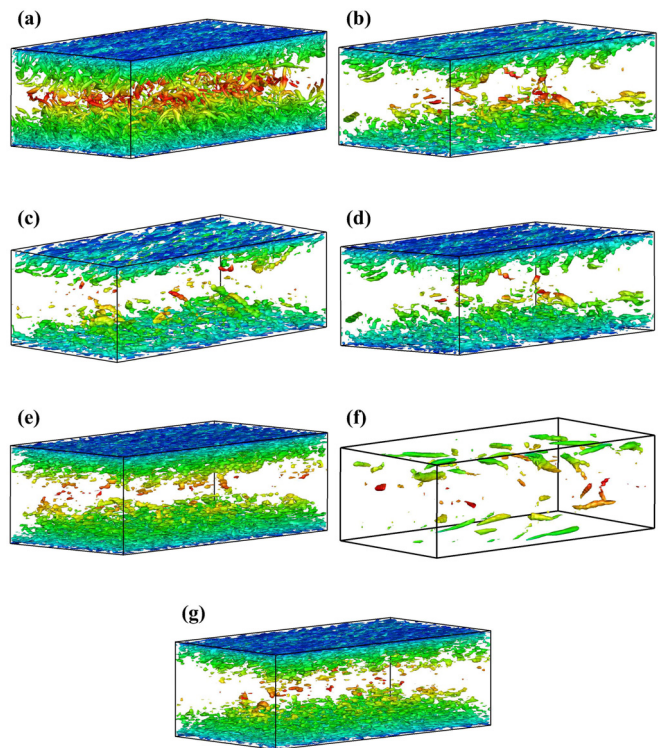


**FIG. 12.** Instantaneous isosurface of  $Q = 350$  obtained from different models in turbulent channel flow of the  $Re_\tau = 395$  (a) DNS, (b)  $dh$ -equation model, (c) DSM, (d)  $dk$ -equation model, (e)  $h$ -equation model, (f) SM, and (g)  $k$ -equation model.

mentioned in the Introduction, helicity could reflect the topological character of the vortex, and it could be inferred that the new models based on SGS helicity can catch finer turbulent structures.

In summary, we propose a new one-equation SGS model based on the SGS helicity. The new LES model can supply better simulation results for incompressible turbulent flows. For future work, it is worth applying the model to transition flow and compressible turbulent flows, which needs further study.

### ACKNOWLEDGMENTS

This work was supported by the National Key Research and Development Program of China (Grant Nos. 2020YFA0711800, 2019YFA0405300, and 2016YFA0401200) and NSFC Projects (Grant Nos. 91852203 and 12072349), National Numerical Windtunnel Project, Science Challenge Project (Grant No. TZ2016001), and Strategic Priority Research Program of Chinese Academy of Sciences (Grant No. XDC01000000). The authors thank the National Supercomputer Center in Tianjin (NSCC-TJ) and the National Supercomputer Center in GuangZhou (NSCC-GZ) for providing computer time.

### DATA AVAILABILITY

The data that support the findings of this study are available from the corresponding author upon reasonable request.

## REFERENCES

- <sup>1</sup>J. Smagorinsky, "General circulation experiments with the primitive equations: I. the basic experiment," *Mon. Weather Rev.* **91**, 99–164 (1963).
- <sup>2</sup>D. Lilly, "On the application of the eddy viscosity concept in the inertial sub-range of turbulence," NCAR Manuscript No. 123 (1967).
- <sup>3</sup>J. P. Chollet and M. Lesieur, "Parameterization of small scales of three-dimensional isotropic turbulence utilizing spectral closures," *J. Atmos. Sci.* **38**, 2747–2757 (1981).
- <sup>4</sup>M. Germano, U. Piomelli, P. Moin, and W. Cabot, "A dynamic subgrid-scale Eddy viscosity model," *Phys. Fluids A* **3**, 1760–1765 (1991).
- <sup>5</sup>F. Nicoud and F. Ducros, "Subgrid-scale stress modelling based on the square of the velocity gradient tensor," *Flow, Turbul. Combust.* **62**(3), 183–200 (1999).
- <sup>6</sup>A. W. Vreman, "An eddy-viscosity subgrid-scale model for turbulent shear flow: Algebraic theory and applications," *Phys. Fluids* **16**, 3670–3681 (2004).
- <sup>7</sup>U. Schumann, "Subgrid scale model for finite difference simulations of turbulent flows in plane channels and annuli," *J. Comput. Phys.* **18**, 376–404 (1975).
- <sup>8</sup>H. K. Yoshizawa, "A statistically-derived subgrid-scale kinetic energy model for the large-eddy simulation of turbulent flows," *J. Phys. Soc. Jpn.* **54**, 2834–2839 (1985).
- <sup>9</sup>S. Ghosal, T. S. Lund, P. Moin, and K. Akselvoll, "A dynamic localization model for large-eddy simulation of turbulent flows," *J. Fluid Mech.* **286**, 229–255 (1995).
- <sup>10</sup>E. Pomraning and C. J. Rutland, "Dynamic one-equation nonviscosity large-eddy simulation model," *AIAA J.* **40**, 689–701 (2002).
- <sup>11</sup>X. Chai and K. Mahesh, "Dynamic-equation model for large-eddy simulation of compressible flows," *J. Fluid Mech.* **699**, 385–413 (2012).
- <sup>12</sup>J. Bardina, J. Ferziger, and W. Reynolds, "Improved subgrid-scale models for large-eddy simulation," 13th Fluid and Plasma Dynamics Conference (1980), p. 1357.
- <sup>13</sup>S. Liu, C. Meneveau, and J. Katz, "On the properties of similarity subgrid-scale models as deduced from measurements in a turbulent jet," *J. Fluid Mech.* **275**, 83–119 (1994).
- <sup>14</sup>P. D. Misra, A., "A vortex-based subgrid model for large-eddy simulation," *Phys. Fluids* **9**, 2443 (1997).
- <sup>15</sup>R. A. Clark, J. H. Ferziger, and W. C. Reynolds, "Evaluation of subgrid-scale models using an accurately simulated turbulent flow," *J. Fluid Mech.* **91**, 1–16 (1979).
- <sup>16</sup>B. Vreman, B. Geurts, and H. Kuerten, "Large-eddy simulation of the temporal mixing layer using the Clark model," *Theor. Comput. Fluid Dyn.* **8**, 309–324 (1996).
- <sup>17</sup>K. Moffatt, "Degree of knottedness of tangled vortex lines," *J. Fluid Mech.* **35**, 117 (1969).
- <sup>18</sup>M. W. Scheeler, W. M. Van Rees, H. Kedia, D. Kleckner, and W. T. M. Irvine, "Complete measurement of helicity and its dynamics in vortex tubes," *Science* **357**, 487–491 (2017).
- <sup>19</sup>Y. A. Yokoi N., "Statistical analysis of the effects of helicity in inhomogeneous turbulence," *Phys. Fluids A* **5**, 464–477 (1993).
- <sup>20</sup>J. Baerenzung, H. Politano, Y. Ponty, and A. Pouquet, "Spectral modeling of turbulent flows and the role of helicity," *Phys. Rev. E* **77**, 046303 (2008).
- <sup>21</sup>C. Yu, R. Hong, Z. Xiao, and S. Chen, "Subgrid-scale eddy viscosity model for helical turbulence," *Phys. Fluids* **25**, 095101 (2013).
- <sup>22</sup>H. Zhou, X. Li, H. Qi, and C. Yu, "Subgrid-scale model for large-eddy simulation of transition and turbulence in compressible flows," *Phys. Fluids* **31**, 125118 (2019).
- <sup>23</sup>Y. Li, C. Meneveau, S. Chen, and G. L. Eyink, "Subgrid-scale modeling of helicity and energy dissipation in helical turbulence," *Phys. Rev. E* **74**, 026310 (2006).
- <sup>24</sup>V. Borue and S. A. Orszag, "Spectra in helical three-dimensional homogeneous isotropic turbulence," *Phys. Rev. E* **55**, 7005–7009 (1997).
- <sup>25</sup>P. Sagaut, *Large Eddy Simulation for Incompressible Flows* (Springer, 2001).
- <sup>26</sup>P. D. V. Nguyen Q., "Using helicity to investigate scalar transport in wall turbulence," *Phys. Rev. Fluids* **5**, 062601 (2020).
- <sup>27</sup>K. Bedford and W. Yeo, "Conjunctive filtering procedures in surface water flow and transport," in *Large Eddy Simulation of Complex Engineering and Geophysical Flows* (Cambridge University Press, 1993), pp. 513–539.
- <sup>28</sup>S. B. Pope, *Turbulent Flows* (Cambridge University Press, 2000).
- <sup>29</sup>U. Schumann, "Realizability of Reynolds-stress turbulence models," *Phys. Fluids* **20**, 721 (1977).
- <sup>30</sup>A. N. Kolmogorov, "Local structure of turbulence in an incompressible liquid for very large Reynolds numbers," *C. R. Acad. Sci., Ser. II* **30**, 301–305 (1941).
- <sup>31</sup>J. Kim, P. Moin, and R. Moser, "Turbulence statistics in fully developed channel flow at low Reynolds number," *J. Fluid Mech.* **177**, 133–166 (1987).
- <sup>32</sup>C. Canuto, M. Yousuff Hussaini, A. Quarteroni, and T. A. Zang, Jr., *Spectral Methods in Fluid Dynamics* (Springer, 1988).
- <sup>33</sup>K. C. Loh and J. A. Domaradzki, "The subgrid-scale estimation model on non-uniform grids," *Phys. Fluids* **11**, 3786–3792 (1999).
- <sup>34</sup>E. van Driest, "On turbulent flow near a wall," *J. Aerosol Sci.* **23**, 1007–1011 (1956).
- <sup>35</sup>J. K. Moser, D. Robert, and N. N. Mansour, "Direct numerical simulation of turbulent channel flow up to  $Re = 590$ ," *Phys. Fluids* **11**, 943–945 (1999).
- <sup>36</sup>J. Meyers and P. Sagaut, "Is plane-channel flow a friendly case for the testing of large-eddy simulation subgrid-scale models?," *Phys. Fluids* **19**, 048105 (2007).
- <sup>37</sup>U. Piomelli, "High Reynolds number calculations using the dynamic subgrid-scale stress model," *Phys. Fluids A* **5**, 1484 (1993).
- <sup>38</sup>J. Jeong and F. Hussain, "On the identification of a vortex," *J. Fluid Mech.* **285**, 69–94 (1995).